INTERNATIONAL JOURNAL FOR NUMERICAL METHODS IN FLUIDS
Int. J. Numer. Meth. Fluids 2005; **48**:1259–1281
Published online 28 April 2005 in Wiley InterScience (www.interscience.wiley.com). DOI: 10.1002/fld.978

Finite-difference 4th-order compact scheme for the direct numerical simulation of instabilities of shear layers

Yan Jiang[‡] and J. M. Floryan[*,†]

Department of Mechanical and Materials Engineering, The University of Western Ontario, London, Ontario, Canada

SUMMARY

An algorithm based on the 4th-order finite-difference compact scheme is developed and applied in the direct numerical simulations of instabilities of channel flow. The algorithm is illustrated in the context of stream function formulation that leads to field equation involving 4th-order spatial derivatives. The finite-difference discretization in the wall-normal direction uses five arbitrarily spaced points. The discretization coefficients are determined numerically, providing a large degree of flexibility for grid selection. The Fourier expansions are used in the streamwise direction. A hybrid Runge–Kutta/Crank–Nicholson low-storage scheme is applied for the time discretization. Accuracy tests demonstrate that the algorithm does deliver the 4th-order accuracy. The algorithm has been used to simulate the natural instability processes in channel flow as well as processes occurring when the flow is spatially modulated using wall transpiration. Extensions to three-dimensional situations are suggested. Copyright © 2005 John Wiley & Sons, Ltd.

KEY WORDS: 4th-order finite-difference compact algorithm; direct numerical simulation; laminar-turbulent transition

1. INTRODUCTION

Many physical processes involve a wide range of spatial scales. A good example is provided by fluid flows in transitional regimes where nonlinear processes lead to the appearance of eddies of different sizes. Simulations of these phenomena require spatial discretization with high resolution and accuracy, i.e. require development of methods that can provide accurate numerical results over as broad a range of length scales as possible for a given discretization.

Spectral methods provide attractive basis for construction of discretization schemes due to their very good resolution properties [1, 2]. One distinctive feature of these methods is

*Correspondence to: J. M. Floryan, Department of Mechanical and Materials Engineering, The University of Western Ontario, London, Ontario, Canada.
†E-mail: mfloryan@eng.uwo.ca
‡E-mail: jiangyan969@yahoo.com

Contract/grant sponsor: NSERC

Received 7 January 2005
Accepted 1 March 2005

that they use infinitely differentiable basis functions. Two common choices are Fourier series expansions and polynomial basis expansions. The global character of the basis functions limits spectral methods to simple geometries and boundary conditions. There is therefore a need to develop methods that provide good geometric flexibility but at the same time retain good resolution properties of the spectral methods [3].

Local numerical representations, such as finite-difference and finite-element, offer the required flexibility in modelling complex geometries and thus variants of such schemes that provide high accuracy and resolution are of interest. These methods use a set of local basis functions without continuity maintained across sub-regions. Spectral finite-element [4, 5] and compact finite-difference [3] provide the relevant examples. Methods based on splines [6] fall somewhere in-between as they use piecewise polynomial representations, but retain a higher degree of continuity. Such methods preserve much of the flexibility afforded by the local expansions while maintain resolution advantage of highly continuous expansions, like spectral methods.

The present work is focused on the development of methods based on finite-differences. High-accuracy traditional (explicit) schemes can be developed by increasing the size of a basic discretization stencil. A more attractive alternative is offered by compact (implicit) schemes as they provide better representation for the shorter length scales. Compact schemes have been used extensively in the past [7, 8] and are of interest in the present work. The coefficients of the finite-difference approximations are derived analytically by matching Taylor expansions of various orders centred at the neighbouring nodes. Detailed analysis of Padé compact schemes, where each derivative is evaluated separately, is given in Reference [3]. One can gain accuracy and resolution by using coupled-derivative formulation, where all derivatives are evaluated simultaneously. Such schemes are particularly attractive when the governing equations involve derivatives of various orders. The case suitable for the Navier–Stokes equations, i.e. system involving first and second derivatives, is discussed in Reference [9].

Detailed descriptions of compact schemes that are available in the literature are limited to uniform grids and schemes based on three nodes in each spatial direction and derivatives up to the 2nd-order [3], as the amount of algebra involved in more general cases becomes insurmountable. Yet, formulations of the flow equations that avoid direct evaluation of pressure lead to the appearance of derivatives up to the 4th-order. Grid redistribution required in order to place more grid points in the areas of high gradients has been achieved by mapping physical domain onto a computational domain and working with a uniform grid there [6], however, mapping suitable for a particular problem may become very complex [10]. Complications associated with the domain decomposition concepts are well illustrated in References [11, 12]. There is a need therefore to develop robust procedures that permit simple implementation of arbitrary nonuniform grids.

Our interest in this work is in the algorithms that are suitable for simulation of the laminar-turbulent transition in spatially modulated flows. The methodology that we have developed follows algorithms described by Spalart *et al.* [13] and Quadrio and Luchini [14, 15]. For simplicity we illustrate the algorithm using stream function formulation as it retains all relevant features of a more general three-dimensional formulation using velocity–vorticity formulation. Section 2 describes the algorithm. In particular, Section 2.1 describes the model problem, Sections 2.2 and 2.3 describe discretization in the streamwise and time directions, respectively, Section 2.4 discusses boundary value problems to be solved at each fractional time step and Section 2.5 describes evaluation of the nonlinear terms required for the advancement to the

next fractional time step. Section 3 provides description of various tests of the complete algorithm. Section 4 discusses extensions to three-dimensional flows. Section 5 provides a short summary of the main conclusions.

2. MODEL PROBLEM AND NUMERICAL ALGORITHM

2.1. Problem formulation

Consider flow confined in a channel bounded by walls at $y = \pm 1$ and extending to $\pm\infty$ in the x-direction as shown in Figure 1. The reference Poiseuille flow is directed along the x-axis and is driven by a pressure gradient. The velocity and pressure fields associated with this flow have the form

$$\vec{v}_0(x, y) = [u_0(y), 0] = [1 - y^2, 0] \tag{1}$$

$$p_0(x, y) = p_0 = -2x/Re \tag{2}$$

where $\vec{v}_0 = (u_0, v_0)$ is the velocity vector, p_0 denotes pressure and Re is the Reynolds number based on the half-channel height and the maximum of x-velocity. The above flow is modified by the wall transpiration in the form of

$$v(x, -1, t) = g_1(x, t) = g_1(x + \lambda_x, t) = \sum_{n=-\infty}^{+\infty} [\hat{g}_1(t)]_n e^{in\alpha x} \tag{3}$$

$$v(x, 1, t) = g_2(x, t) = g_2(x + \lambda_x, t) = \sum_{n=-\infty}^{+\infty} [\hat{g}_2(t)]_n e^{in\alpha x} \tag{4}$$

applied at the lower and upper walls, respectively. It is assumed that g_1 and g_2 are periodic in the x-direction, with $\lambda_x = 2\pi/\alpha$ denoting the wavelength of one period and α standing for the wave number. It is further assumed that the net mass flow rates associated with both transpirations are identical and directed in the opposite sense so that the transpiration does not contribute to the net mass flow in the x-direction.

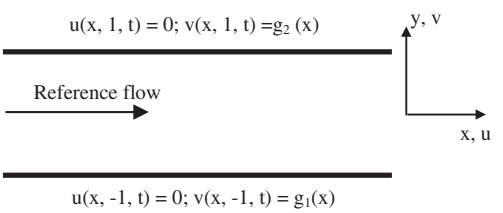

Figure 1. Schematic diagram of the channel flow.

The velocity and pressure fields in the channel with transpiration can be written as

$$\vec{v}(x,y,t) = \vec{v}_0(y) + \vec{v}'(x,y,t) \tag{5}$$

$$p(x,y,t) = p_0(x) + p'(x,y,t) \tag{6}$$

where $\vec{v}'(x,y,t)$ and $p'(x,y,t)$ describe velocity and pressure modifications due to the transpiration, respectively, and $\vec{v}(x,y,t) = [u(x,y,t), v(x,y,t)]$ and $p(x,y,t)$ denote the total velocity vector and the total pressure.

It is sometimes advantageous to carry out computations in a moving frame of reference. The problem formulation is thus generalized by introducing frame (X, y) moving with a constant velocity c with respect to the laboratory frame (x, y), i.e. $X = x - ct$. The governing equations written in this frame have the form

$$\frac{\partial u}{\partial X} + \frac{\partial v}{\partial y} = 0 \tag{7a}$$

$$\frac{\partial u}{\partial t} - c\frac{\partial u}{\partial X} + u\frac{\partial u}{\partial X} + v\frac{\partial u}{\partial y} = -\frac{\partial p}{\partial X} + \frac{1}{Re}(\nabla^2 u) \tag{7b}$$

$$\frac{\partial v}{\partial t} - c\frac{\partial v}{\partial X} + u\frac{\partial v}{\partial X} + v\frac{\partial v}{\partial y} = -\frac{\partial p}{\partial y} + \frac{1}{Re}(\nabla^2 v) \tag{7c}$$

where $\nabla^2 = \partial^2/\partial X^2 + \partial^2/\partial y^2$. Boundary conditions written in the moving frame have the form

$$v(X,-1,t) = g_1(X + ct, t) = G_1(X,t) \tag{7d}$$

$$v(X,1,t) = g_2(X + ct, t) = G_2(X,t) \tag{7e}$$

$$u(X,\pm 1,t) = 0 \tag{7f}$$

Introduction of the stream function defined as $u = u_0 + \partial\varphi/\partial y$ and $v = -\partial\varphi/\partial X$ permits combination of the momentum transport equations into a single equation in the form

$$\frac{\partial}{\partial t}(\nabla^2\varphi) = \frac{1}{Re}\nabla^2(\nabla^2\varphi) + c\frac{\partial}{\partial X}(\nabla^2\varphi) - \frac{\partial}{\partial y}\left(\frac{\partial\langle uu\rangle}{\partial X} + \frac{\partial\langle uv\rangle}{\partial y}\right) + \frac{\partial}{\partial X}\left(\frac{\partial\langle uv\rangle}{\partial X} + \frac{\partial\langle vv\rangle}{\partial y}\right) \tag{8a}$$

where $\langle uu\rangle = uu, \langle uv\rangle = \langle vu\rangle = uv, \langle vv\rangle = vv$.

Boundary conditions in the y-directions for Equation (8a) can be written as

$$\left.\frac{\partial\varphi}{\partial y}\right|_{y=\pm 1} = 0 \tag{8b–c}$$

$$\left.\frac{\partial\varphi}{\partial X}\right|_{y=-1} = -G_1(X,t) = -g_1(X + ct, t) = \sum_{n=-\infty}^{n=+\infty} [\hat{g}_1(t)]_n e^{in\alpha(X+ct)} \tag{8d}$$

$$\left.\frac{\partial\varphi}{\partial X}\right|_{y=+1} = -G_2(X,t) = -g_2(X+ct,t) = \sum_{n=-\infty}^{n=+\infty} [\hat{g}_2(t)]_n \mathrm{e}^{\mathrm{i}n\alpha(X+ct)} \tag{8e}$$

The reader may note that the velocity field needs to satisfy periodicity condition in the X-direction due to the periodicity of the wall transpiration. The pressure field may have, in general, a linear component in X-direction in addition to the periodic components. Further, one needs to note that the use of stream function introduces an arbitrary constant into the problem formulation.

2.2. Spectral discretization in the streamwise direction

Solution of Equations (8a)–(8e) is expressed in the form of Fourier expansions in the streamwise direction, where the variables with hat denote the Fourier modal functions, e.g.

$$\varphi(X,y,t) = \sum_{n=-\infty}^{\infty} \hat{\varphi}_n(y,t)\mathrm{e}^{\mathrm{i}\alpha nX} \tag{9a}$$

$$u(X,y,t) = u_0(y) + \sum_{n=-\infty}^{\infty} \hat{u}_n(y,t)\mathrm{e}^{\mathrm{i}\alpha nX} \tag{9b}$$

$$v(X,y,t) = \sum_{n=-\infty}^{\infty} \hat{v}_n(y,t)\mathrm{e}^{\mathrm{i}\alpha nX} \tag{9c}$$

$$\langle uu\rangle(X,y,t) = \sum_{n=-\infty}^{\infty} [\langle u\hat{u}\rangle_n(y,t)]\mathrm{e}^{\mathrm{i}\alpha nX} \tag{9d}$$

$$\langle uv\rangle(X,y,t) = \sum_{n=-\infty}^{\infty} [\langle u\hat{v}\rangle_n(y,t)]\mathrm{e}^{\mathrm{i}\alpha nX} \tag{9e}$$

$$\langle vv\rangle(X,y,t) = \sum_{n=-\infty}^{\infty} [\langle v\hat{v}\rangle_n(y,t)]\mathrm{e}^{\mathrm{i}\alpha nX} \tag{9f}$$

The momentum transport equation (7a) can be expressed in terms of the modal functions in the form of

$$\frac{\partial}{\partial t}[(D^2-\alpha^2n^2)\hat{\varphi}_n] = \frac{1}{Re}D^4\hat{\varphi}_n + \left(i\alpha nc - \frac{2}{Re}\alpha^2n^2\right)D^2\hat{\varphi}_n + \left(\frac{1}{Re}\alpha^4n^4 - ic\alpha^3n^3\right)\hat{\varphi}_n$$
$$+ i\alpha n[i\alpha n(\langle\hat{u}\hat{v}\rangle_n) + D\langle\hat{v}\hat{v}\rangle_n] - in\alpha D(\langle\hat{u}\hat{u}\rangle_n) - D^2(\langle\hat{u}\hat{v}\rangle_n) \tag{10a}$$

where $D^4 = \mathrm{d}^4/\mathrm{d}y^4$, $D^2 = \mathrm{d}^2/\mathrm{d}y^2$, $D = \mathrm{d}/\mathrm{d}y$. The boundary conditions take the form

$$\text{at } y=-1,\ \hat{\varphi}_n(y,t) = \frac{i(\hat{g}_1)_n\mathrm{e}^{\mathrm{i}\alpha nct}}{n\alpha} \text{ for } n\neq 0, \quad \hat{\varphi}_0(-1,t)=0 \quad \text{for } n=0 \tag{10b}$$

$$\text{at } y=1,\ \hat{\varphi}_n(y,t) = \frac{i(\hat{g}_2)_n\mathrm{e}^{\mathrm{i}\alpha nct}}{n\alpha} \text{ for } n\neq 0, \quad \hat{\varphi}_0(1,t)=Q-\tfrac{4}{3} \text{ for } n=0 \tag{10c}$$

$$\text{at } y = \pm 1, \quad \frac{\mathrm{d}\hat{\varphi}_n}{\mathrm{d}y} = 0 \tag{10d–e}$$

where Q denotes the total mass flow of the transpiration-modified flow. The reader may note that there are no natural boundary conditions for mode $n = 0$ which corresponds to the existence of a linear component in the pressure field. This component is determined in the present work by imposing constant mass flow rate constrain. When the total mass flow is to remain the same as the mass flow of the Poiseuille flow, one must take $Q = \frac{4}{3}$. The conditions for $n = 0$ form a pair that determines the value of the arbitrary constant associated with the introduction of the stream function as well as imposes the mass flow rate constrain.

2.3. Time discretization

Three-step hybrid Runge–Kutta/Crank–Nicholson low-storage scheme [13, 16] is applied for time discretization. The main idea of this scheme is that the 2nd-order Crank–Nicholson method is applied to the viscous terms and the three-step low-storage Runge–Kutta scheme is applied to the convective terms. The time-dependent momentum transport equation can be written in a generic form

$$\frac{\partial f}{\partial t} = L(f) + N(f) \tag{11a}$$

where f represents the unknown variable, L is a linear operator, N is a nonlinear operator, and L and N do not depend on time. The scheme to advance from f^n, at the time t, to f^{n+1}, at time $t + \Delta t$, has three sub-steps

$$f^{n+1/3} = f^n + \Delta t\,[L(\kappa_1 f^n + \tau_1 f^{n+1/3}) + \gamma_1 N^n] \tag{11b}$$

$$f^{n+2/3} = f^{n+1/3} + \Delta t\,[L(\kappa_2 f^{n+1/3} + \tau_2 f^{n+2/3}) + \gamma_2 N^{n+1/3} + \zeta_1 N^n] \tag{11c}$$

$$f^{n+1} = f^{n+2/3} + \Delta t[L(\kappa_3 f^{n+2/3} + \tau_3 f^{n+1}) + \gamma_3 N^{n+2/3} + \zeta_2 N^{n+1/3}] \tag{11d}$$

where $\tau_1 = \frac{37}{160}$, $\tau_2 = \frac{5}{24}$, $\tau_3 = \frac{1}{6}$, $\kappa_1 = \frac{29}{96}$, $\kappa_2 = \frac{3}{40}$, $\kappa_3 = \frac{1}{6}$, $\gamma_1 = \frac{8}{15}$, $\gamma_2 = \frac{5}{12}$, $\gamma_3 = \frac{3}{4}$, $\zeta_1 = -\frac{17}{60}$, $\zeta_2 = -\frac{5}{12}$. Determination of the unknown f at each fractional time step involves solution of a boundary value problem. The nonlinear terms are considered to be known and are evaluated using FFT algorithm. Aliasing errors are eliminated by implementation of the padding method [1].

2.4. Boundary value problems at a fractional time step

The boundary value problems at each fractional time step have the generic form of

$$b_1 D^4 f(y) + b_2 D^2 f(y) + b_3 D f(y) + b_4 f(y) = g(y) \tag{12}$$

where b_1, b_2, b_3 and b_4 are known constant coefficients and $g(y)$ is a known function. The detailed forms of the coefficients and the boundary conditions for each fractional time step are presented in Appendix A.

We wish to solve the above problem with high accuracy using finite-difference approximations on arbitrary distributed grid points. The main difficulty is associated with the presence

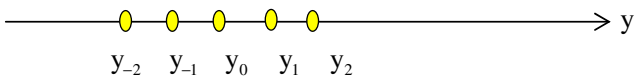

Figure 2. Schematic diagram of the five-point stencil used for the discretization.

of the 4th-derivative. Below, we described a 4th-order compact scheme that satisfies our requirements.

The 4th-order compact finite-difference scheme is built on a five-point-stencil shown in Figure 2. Approximation for grid point y_0 is constructed by writing Equation (12) at the five points of the stencil and adding the results with appropriate weights $d_i^{(0)}$. The result has the form

$$b_1 \sum_{i=-2}^{2} d_i^{(0)} D^4 f(y_i) + b_2 \sum_{i=-2}^{2} d_i^{(0)} D^2 f(y_i) + b_3 \sum_{i=-2}^{2} d_i^{(0)} D f(y_i) + b_4 \sum_{i=-2}^{2} d_i^{(0)} f(y_i)$$

$$= \sum_{i=-2}^{2} d_i^{(0)} g(y_i) \tag{13}$$

Derivatives in the above equation can be expressed in terms of the unknown function by imposing the following relations:

$$\sum_{i=-2}^{2} d_i^{(4)} f(y_i) = \sum_{i=-2}^{2} d_i^{(0)} D^4 f(y_i) \tag{14a}$$

$$\sum_{i=-2}^{2} d_i^{(2)} f(y_i) = \sum_{i=-2}^{2} d_i^{(0)} D^2 f(y_i) \tag{14b}$$

$$\sum_{i=-2}^{2} d_i^{(1)} f(y_i) = \sum_{i=-2}^{2} d_i^{(0)} D f(y_i) \tag{14c}$$

where the weights $d_i^{(4)}$, $d_i^{(2)}$, $d_i^{(1)}$ and $d_i^{(0)}$ are to be selected in such a way that the scheme provides a minimum of 4th-order accuracy. This is accomplished by enforcing these equations to be satisfied exactly by polynomials $1, y, y^2, y^3$, etc. Weights $d_i^{(4)}$ and $d_i^{(0)}$ are selected from Equation (14a) using polynomials up to order eight resulting in a system of nine algebraic equations. This system is supplemented by a normalization condition providing ten degrees of freedom for the approximation of the 4th-derivative. The normalization conditions can be selected in such a way that the system separates into two systems of five equations each, with one of them describing $d_i^{(4)}$ and the other one describing $d_i^{(0)}$. These systems have the following form:

$$d_{-2}^{(4)} + d_{-1}^{(4)} + d_0^{(4)} + d_1^{(4)} + d_2^{(4)} = 0 \tag{15a}$$

$$d_{-2}^{(4)}\delta_{-2} + d_{-1}^{(4)}\delta_{-1} + d_1^{(4)}\delta_1 + d_2^{(4)}\delta_2 = 0 \tag{15b}$$

$$d_{-2}^{(4)}\delta_{-2}^2 + d_{-1}^{(4)}\delta_{-1}^2 + d_1^{(4)}\delta_1^2 + d_2^{(4)}\delta_2^2 = 0 \tag{15c}$$

$$d_{-2}^{(4)}\delta_{-2}^3 + d_{-1}^{(4)}\delta_{-1}^3 + d_1^{(4)}\delta_1^3 + d_2^{(4)}\delta_2^3 = 0 \tag{15d}$$

$$d_{-2}^{(4)}\delta_{-2}^4 + d_{-1}^{(4)}\delta_{-1}^4 + d_1^{(4)}\delta_1^4 + d_2^{(4)}\delta_2^4 = 24 \tag{15e}$$

$$d_{-2}^{(0)} + d_{-1}^{(0)} + d_0^{(0)} + d_1^{(0)} + d_2^{(0)} = 1 \tag{16a}$$

$$120(d_{-2}^{(0)}\delta_{-2} + d_{-1}^{(0)}\delta_{-1} + d_1^{(0)}\delta_1 + d_2^{(0)}\delta_2) = d_{-2}^{(4)}\delta_{-2}^5 + d_{-1}^{(4)}\delta_{-1}^5 + d_1^{(4)}\delta_1^5 + d_2^{(4)}\delta_2^5 \tag{16b}$$

$$360(d_{-2}^{(0)}\delta_{-2}^2 + d_{-1}^{(0)}\delta_{-1}^2 + d_1^{(0)}\delta_1^2 + d_2^{(0)}\delta_2^2) = d_{-2}^{(4)}\delta_{-2}^6 + d_{-1}^{(4)}\delta_{-1}^6 + d_1^{(4)}\delta_1^6 + d_2^{(4)}\delta_2^6 \tag{16c}$$

$$840(d_{-2}^{(0)}\delta_{-2}^3 + d_{-1}^{(0)}\delta_{-1}^3 + d_1^{(0)}\delta_1^3 + d_2^{(0)}\delta_2^3) = d_{-2}^{(4)}\delta_{-2}^7 + d_{-1}^{(4)}\delta_{-1}^7 + d_1^{(4)}\delta_1^7 + d_2^{(4)}\delta_2^7 \tag{16d}$$

$$1680(d_{-2}^{(0)}\delta_{-2}^4 + d_{-1}^{(0)}\delta_{-1}^4 + d_1^{(0)}\delta_1^4 + d_2^{(0)}\delta_2^4) = d_{-2}^{(4)}\delta_{-2}^8 + d_{-1}^{(4)}\delta_{-1}^8 + d_1^{(4)}\delta_1^8 + d_2^{(4)}\delta_2^8 \tag{16e}$$

where Equation (16a) describes the normalization condition and $\delta_j = y_j - y_0$. Solution of (15) for $d_i^{(4)}$, which is decoupled from (16), is carried out numerically. This system is ill-posed and thus it is difficult to produce its accurate solution, especially when grid spacing becomes very small; these difficulties are easily overcome by arbitrary accuracy arithmetic (rather than the usual 64-bit arithmetic associated with the double precision representation of computer words). Solutions of all linear systems for weights described in this paper have been carried out using arbitrary accuracy arithmetic. Solution of (16) for $d_i^{(0)}$ is determined once $d_i^{(4)}$ have been found. Weights $d_i^{(2)}$ are selected in a similar manner using the already determined weights $d_i^{(0)}$ and thus providing five degrees of freedom for the approximation of the 2nd derivative. The corresponding equation has the form

$$d_{-2}^{(2)} + d_{-1}^{(2)} + d_0^{(2)} + d_1^{(2)} + d_2^{(2)} = 0 \tag{17a}$$

$$d_{-2}^{(2)}\delta_{-2} + d_{-1}^{(2)}\delta_{-1} + d_1^{(2)}\delta_1 + d_2^{(2)}\delta_2 = 0 \tag{17b}$$

$$d_{-2}^{(2)}\delta_{-2}^2 + d_{-1}^{(2)}\delta_{-1}^2 + d_1^{(2)}\delta_1^2 + d_2^{(2)}\delta_2^2 = 2(d_{-2}^{(0)} + d_{-1}^{(0)} + d_1^{(0)} + d_2^{(0)}) \tag{17c}$$

$$d_{-2}^{(2)}\delta_{-2}^3 + d_{-1}^{(2)}\delta_{-1}^3 + d_1^{(2)}\delta_1^3 + d_2^{(2)}\delta_2^3 = 6(d_{-2}^{(0)}\delta_{-2} + d_{-1}^{(0)}\delta_{-1} + d_1^{(0)}\delta_1 + d_2^{(0)}\delta_2) \tag{17d}$$

$$d_{-2}^{(2)}\delta_{-2}^4 + d_{-1}^{(2)}\delta_{-1}^4 + d_1^{(2)}\delta_1^4 + d_2^{(2)}\delta_2^4 = 12(d_{-2}^{(0)}\delta_{-2}^2 + d_{-1}^{(0)}\delta_{-1}^2 + d_1^{(0)}\delta_1^2 + d_2^{(0)}\delta_2^2) \tag{17e}$$

Determination of weights $d_i^{(1)}$ follows the same pattern providing five degrees of freedom for the approximation of the first derivative and resulting in the following system of equations:

$$d_{-2}^{(1)} + d_{-1}^{(1)} + d_0^{(1)} + d_1^{(1)} + d_2^{(1)} = 0 \tag{18a}$$

$$d_{-2}^{(1)}\delta_{-2} + d_{-1}^{(1)}\delta_{-1} + d_1^{(1)}\delta_1 + d_2^{(1)}\delta_2 = d_{-2}^{(0)} + d_{-1}^{(0)} + d_0^{(0)} + d_1^{(0)} + d_2^{(0)} \tag{18b}$$

$$d_{-2}^{(1)}\delta_{-2}^2 + d_{-1}^{(1)}\delta_{-1}^2 + d_1^{(1)}\delta_1^2 + d_2^{(1)}\delta_2^2 = 2(d_{-2}^{(0)}\delta_{-2} + d_{-1}^{(0)}\delta_{-1} + d_1^{(0)}\delta_1 + d_2^{(0)}\delta_2) \tag{18c}$$

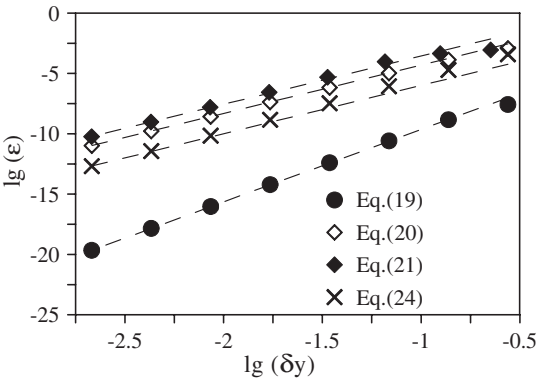

Figure 3. Variations of the error $\varepsilon = |f_{\text{exact}} - f_{\text{computed}}|$ at $y = 0.5$ as a function of the grid size δy. Numerical solution of Equations (19)–(21) has been carried out with the explicit evaluation of the boundary values, while full numerical treatment of boundary conditions was used in the case of Equation (24). The initial grid consisting of ten points located at $y = 0, 0.3, 0.5, 0.85, 0.95, 1.11, 1.25, 1.35, 1.52, 1.9, 2$ was refined in the test through sequential halving of the distance between the neighbouring points. Additional points at $y = -0.2$ and 2.2 were used for Equation (24). δy denotes the average distance between the grid points.

$$d_{-2}^{(1)}\delta_{-2}^3 + d_{-1}^{(1)}\delta_{-1}^3 + d_1^{(1)}\delta_1^3 + d_2^{(1)}\delta_2^3 = 3(d_{-2}^{(0)}\delta_{-2}^2 + d_{-1}^{(0)}\delta_{-1}^2 + d_1^{(0)}\delta_1^2 + d_2^{(0)}\delta_2^2) \quad (18d)$$

$$d_{-2}^{(1)}\delta_{-2}^4 + d_{-1}^{(1)}\delta_{-1}^4 + d_1^{(1)}\delta_1^4 + d_2^{(1)}\delta_2^4 = 4(d_{-2}^{(0)}\delta_{-2}^3 + d_{-1}^{(0)}\delta_{-2}^3 + d_1^{(0)}\delta_1^3 + d_2^{(0)}\delta_2^3) \quad (18e)$$

Equations (16)–(18) are solved numerically for the unknown weights for the selected grid distribution. The resulting numerical overhead is very minimal as compared to the overall cost of the computations as the weights need to be determined only once [17].

The above discretization scheme is in-between Padé and coupled derivative formulations and can be easily re-arranged to produce each formulation explicitly. Accuracies of different elements of the formulation have been tested separately on an intentionally highly nonuniform grid (see Figure 3). To test representation of the 4th derivative, we solve differential equation in the form

$$D^4 f = \exp(y) - 8\cos(2y), \quad y \in \langle 0, 1 \rangle \quad (19)$$

whose exact solution is $f(y) = \exp(y) + \sin^2(y)$. In order to avoid problems with numerical implementation of boundary conditions we utilize exact values of the solution at two neighbouring points at the ends of the solution domain so that our five-point scheme can be applied directly. Plot of error variations as a function of grid size shown in Figure 3 demonstrates that the scheme provides 6th-order accuracy for the 4th derivative. A similar test for the 2nd derivative utilizes equation in the form

$$D^2 f = \exp(y) + 2\cos(2y), \quad y \in \langle 0, 1 \rangle \quad (20)$$

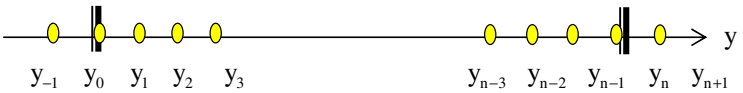

Figure 4. Schematic diagram of stencils used around the boundaries of the solution domain.

whose exact solution is $f(y) = \exp(y) + \sin^2(y)$. Results displayed in Figure 3 demonstrate the 4th-order accuracy. Test for the 1st derivative utilizes equation in the form

$$Df = \exp(y) + \sin(2y), \quad y \in \langle 0, 1 \rangle \tag{21}$$

whose exact solution is $f(y) = \exp(y) + \sin^2(y)$. Figure 3 demonstrates 4th-order of accuracy of this scheme.

The discretization schemes described above can be applied only at the central point of the stencil and thus are not suitable for points located next to the boundaries of the solution domain. Since the overall accuracy of the finite-difference discretization of Equation (12) is of the 4th-order (as dictated by the accuracy of the 1st and 2nd derivatives), it is sufficient to develop 4th-order accurate treatment of points adjacent to the boundaries as well boundary conditions themselves.

The relevant stencil applied around the boundaries is shown in Figure 4. We shall limit our discussion to the left end, as treatment of the right end is identical. Equation (12) is discretized at point y_1 in the same way as in all other internal points and this brings in a new unknown in the form of $f(y_{-1})$. The boundary condition for the function is applied directly at point y_0 while the boundary condition for the derivative is used to construct equation for $f(y_{-1})$. The 4th-order representation of the first derivative at point y_0 using points $-1, 0, \ldots, 3$ is developed on the basis of relation

$$\sum_{j=-1}^{3} d^{(1)}_{\text{left},j} f(y_j) = Df(y_0) \tag{22}$$

where the weights $d^{(1)}_{\text{left},j}$ are selected by forcing Equation (22) to be satisfied by polynomials up to order four. This leads to a system of five linear equations in the form

$$d^{(1)}_{\text{left},-1} + d^{(1)}_{\text{left},0} + d^{(1)}_{\text{left},1} + d^{(1)}_{\text{left},2} + d^{(1)}_{\text{left},3} = 0 \tag{23a}$$

$$d^{(1)}_{\text{left},-1}\delta_{-1} + d^{(1)}_{\text{left},1}\delta_1 + d^{(1)}_{\text{left},2}\delta_2 + d^{(1)}_{\text{left},3}\delta_3 = 0 \tag{23b}$$

$$d^{(1)}_{\text{left},-1}\delta^2_{-1} + d^{(1)}_{\text{left},1}\delta^2_1 + d^{(1)}_{\text{left},2}\delta^2_2 + d^{(1)}_{\text{left},3}\delta^2_3 = 0 \tag{23c}$$

$$d^{(1)}_{\text{left},-1}\delta^3_{-1} + d^{(1)}_{\text{left},1}\delta^3_1 + d^{(1)}_{\text{left},2}\delta^3_2 + d^{(1)}_{\text{left},3}\delta^3_3 = 6 \tag{23d}$$

$$d^{(1)}_{\text{left},-1}\delta^4_{-1} + d^{(1)}_{\text{left},1}\delta^4_1 + d^{(1)}_{\text{left},2}\delta^4_2 + d^{(1)}_{\text{left},3}\delta^4_3 = 0 \tag{23e}$$

which is solved numerically for the weights.

One can write equations of type (13) for each interior grid point and supplement them with two boundary conditions of type (22) to construct a system of equations for the unknown

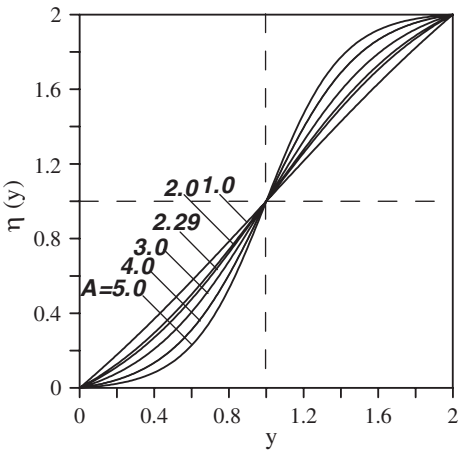

Figure 5. Effect of the parameter A on the grid nonuniformity (see Equation (25)).

function f, with the resulting matrix of coefficients having banded structure with the band width of five.

We carry out numerical testing of the accuracy of the solution of a complete equation similar to Equation(12) using model equation

$$D^4 f + D^2 f + Df + f = 4\exp(y) + \sin(2y) - 6\cos(2y) + (\sin(y))^2, \quad y \in (0,2) \tag{24}$$

whose exact solution has the form $f(y) = \exp(y) + (\sin(y))^2$. The boundary conditions for f and Df at $y = 0, 2$ are determined by evaluating exact solution at these points. Results displayed in Figure 3 demonstrate that the algorithm delivers the 4th-order accuracy.

The absolute accuracy can be improved through a suitable distribution of the grid points. This distribution can be changed, for example, using formula in the form

$$\eta(y) = \tanh(Ay/2)/\tanh(A/2) \tag{25}$$

with A being a parameter. Results displayed in Figure 4 demonstrate that an increase of the value of A results in a larger concentration of grid points around the boundaries.

Variations of the maximum error for different grid distributions, as characterized by the parameter A, are displayed in Figure 5. It can be seen that a suitable selection of A can result in the error reduction by almost two orders of magnitude without any additional computational cost.

2.5. Data processing at the end of each fractional time step

The boundary value problem at a fractional time step (Equation (12)) involves known function $g(y)$ on the right-hand side. This function has to be updated between different fractional time steps, which necessitate numerical evaluation of the 1st, 2nd and 3rd derivatives of the numerically determined function f (stream function). The structure of the overall algorithm is such that higher derivatives are evaluated through a repeated evaluation of the 1st derivative. The numerical differentiation has to provide a minimum of 4th-order accuracy for all required derivatives.

The required accuracy of a single differentiation is provided through an implicit differentiation procedure. The five-points stencil shown in Figure 2 is used at the internal grid points where relation in the form

$$\sum_{j=-2}^{2} c_j^{(1)} f(y_j) = \sum_{j=-2}^{2} c_j^{(0)} Df(y_j) \tag{26}$$

is used. The unknown weight $c_j^{(1)}$ and $c_j^{(0)}$ are evaluated by forcing the above relation to be satisfied by polynomials up to order eight which leads to nine relations. Addition of a normalization condition leads to a system of ten equations in the form

$$c_{-2}^{(1)} + c_{-1}^{(1)} + c_0^{(1)} + c_1^{(1)} + c_2^{(1)} = 0 \tag{27a}$$

$$c_{-2}^{(1)}\delta_{-2} + c_{-1}^{(1)}\delta_{-1} + c_1^{(1)}\delta_1 + c_2^{(1)}\delta_2 = c_{-2}^{(0)} + c_{-1}^{(0)} + c_0^{(0)} + c_1^{(0)} + c_2^{(0)} \tag{27b}$$

$$c_{-2}^{(1)}\delta_{-2}^2 + c_{-1}^{(1)}\delta_{-1}^2 + c_1^{(1)}\delta_1^2 + c_2^{(1)}\delta_2^2 = 2(c_{-2}^{(0)}\delta_{-2} + c_{-1}^{(0)}\delta_{-1} + c_1^{(0)}\delta_1 + c_2^{(0)}\delta_2) \tag{27c}$$

$$c_{-2}^{(1)}\delta_{-2}^3 + c_{-1}^{(1)}\delta_{-1}^3 + c_1^{(1)}\delta_1^3 + c_2^{(1)}\delta_2^3 = 3(c_{-2}^{(0)}\delta_{-2}^2 + c_{-1}^{(0)}\delta_{-1}^2 + c_1^{(0)}\delta_1^2 + c_2^{(0)}\delta_2^2) \tag{27d}$$

$$c_{-2}^{(1)}\delta_{-2}^4 + c_{-1}^{(1)}\delta_{-1}^4 + c_1^{(1)}\delta_1^4 + c_2^{(1)}\delta_2^4 = 4(c_{-2}^{(0)}\delta_{-2}^3 + c_{-1}^{(0)}\delta_{-1}^3 + c_1^{(0)}\delta_1^3 + c_2^{(0)}\delta_2^3) \tag{27e}$$

$$c_{-2}^{(1)}\delta_{-2}^5 + c_{-1}^{(1)}\delta_{-1}^5 + c_1^{(1)}\delta_1^5 + c_2^{(1)}\delta_2^5 = 5(c_{-2}^{(0)}\delta_{-2}^4 + c_{-1}^{(0)}\delta_{-1}^4 + c_1^{(0)}\delta_1^4 + c_2^{(0)}\delta_2^4) \tag{27f}$$

$$c_{-2}^{(1)}\delta_{-2}^6 + c_{-1}^{(1)}\delta_{-1}^6 + c_1^{(1)}\delta_1^6 + c_2^{(1)}\delta_2^6 = 6(c_{-2}^{(0)}\delta_{-2}^5 + c_{-1}^{(0)}\delta_{-1}^5 + c_1^{(0)}\delta_1^5 + c_2^{(0)}\delta_2^5) \tag{27g}$$

$$c_{-2}^{(1)}\delta_{-2}^7 + c_{-1}^{(1)}\delta_{-1}^7 + c_1^{(1)}\delta_1^7 + c_2^{(1)}\delta_2^7 = 7(c_{-2}^{(0)}\delta_{-2}^6 + c_{-1}^{(0)}\delta_{-1}^6 + c_1^{(0)}\delta_1^6 + c_2^{(0)}\delta_2^6) \tag{27h}$$

$$c_{-2}^{(1)}\delta_{-2}^8 + c_{-1}^{(1)}\delta_{-1}^8 + c_1^{(1)}\delta_1^8 + c_2^{(1)}\delta_2^8 = 7(c_{-2}^{(0)}\delta_{-2}^7 + c_{-1}^{(0)}\delta_{-1}^7 + c_1^{(0)}\delta_1^7 + c_2^{(0)}\delta_2^7) \tag{27i}$$

$$c_{-2}^{(0)} + c_{-1}^{(0)} + c_0^{(0)} + c_1^{(0)} + c_2^{(0)} = 1 \tag{27j}$$

with the last relation playing the role of the normalization condition.

Equation (26) has to be supplemented by special relations for boundary points $-1, 0, n, n+1$ in Figure 4. We shall limit our discussion to the points on the left boundary only. At point zero we use relation in the form

$$\sum_{j=0}^{3} c_{\text{left},j}^{(1)} f(y_j) = \sum_{j=0}^{3} c_{\text{left},j}^{(0)} Df(y_j) \tag{28}$$

that utilizes data from points $0, \ldots, 3$. The weights are determined by enforcing the above relation for polynomials up to 6th-order, which leads a system of eight linear equations in the form

$$c_{\text{left},0}^{(1)} + c_{\text{left},1}^{(1)} + c_{\text{left},2}^{(1)} + c_{\text{left},3}^{(1)} = 0 \tag{29a}$$

$$c_{\text{left},1}^{(1)}\delta_1 + c_{\text{left},2}^{(1)}\delta_2 + c_{\text{left},3}^{(1)}\delta_3 = c_{\text{left},0}^{(0)} + c_{\text{left},1}^{(0)} + c_{\text{left},2}^{(0)} + c_{\text{left},3}^{(0)} \tag{29b}$$

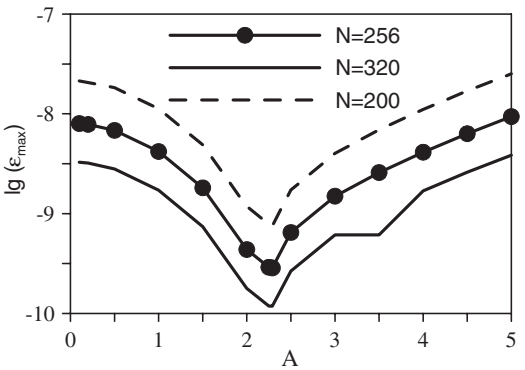

Figure 6. Variations of the maximum error of the numerical solution of Equation (24) as a function of the grid nonuniformity characterized by the parameter A (see Equation (25)). N represents the total number of grid points used.

$$c^{(1)}_{\text{left},1}\delta_1^2 + c^{(1)}_{\text{left},2}\delta_2^2 + c^{(1)}_{\text{left},3}\delta_3^2 = 2(c^{(0)}_{\text{left},1}\delta_1 + c^{(0)}_{\text{left},2}\delta_2 + c^{(0)}_{\text{left},3}\delta_3) \tag{29c}$$

$$c^{(1)}_{\text{left},1}\delta_1^3 + c^{(1)}_{\text{left},2}\delta_2^3 + c^{(1)}_{\text{left},3}\delta_3^3 = 3(c^{(0)}_{\text{left},1}\delta_1^2 + c^{(0)}_{\text{left},2}\delta_2^2 + c^{(0)}_{\text{left},3}\delta_3^2) \tag{29d}$$

$$c^{(1)}_{\text{left},1}\delta_1^4 + c^{(1)}_{\text{left},2}\delta_2^4 + c^{(1)}_{\text{left},3}\delta_3^4 = 4(c^{(0)}_{\text{left},1}\delta_1^3 + c^{(0)}_{\text{left},2}\delta_2^3 + c^{(0)}_{\text{left},3}\delta_3^3) \tag{29e}$$

$$c^{(1)}_{\text{left},1}\delta_1^5 + c^{(1)}_{\text{left},2}\delta_2^5 + c^{(1)}_{\text{left},3}\delta_3^5 = 5(c^{(0)}_{\text{left},1}\delta_1^4 + c^{(0)}_{\text{left},2}\delta_2^4 + c^{(0)}_{\text{left},3}\delta_3^4) \tag{29f}$$

$$c^{(1)}_{\text{left},1}\delta_1^6 + c^{(1)}_{\text{left},2}\delta_2^6 + c^{(1)}_{\text{left},3}\delta_3^6 = 6(c^{(0)}_{\text{left},1}\delta_1^5 + c^{(0)}_{\text{left},2}\delta_2^5 + c^{(0)}_{\text{left},3}\delta_3^5) \tag{29g}$$

$$c^{(1)}_{\text{left},0} = 1 \tag{29h}$$

where the last equation plays the role of the normalization condition and $\delta_1 = y_1 - y_0$, $\delta_2 = y_2 - y_0$, $\delta_3 = y_3 - y_0$. The above system is solved numerically for the unknown weights. Similar relation has been developed for point -1 in Figure 4 using data from points $-1, 0, 1, 2$.

Use of formula (27) at all internal grid points and formulae of type (29) at the four boundary points leads to a system of linear equations describing the unknown derivative. The reader may note that the first differentiation of the function f (equivalent to the evaluation of the streamwise velocity component u) can be simplified by taking advantage of the known value of Df at the wall, which leads to a system of equations with banded matrix of coefficients with band width five. The second differentiation (equivalent to the evaluation of Du) leads to a banded matrix with band width seven. Similar situation exist in the third differentiation (equivalent to the evaluation of D^2u).

Two types of tests have been used to verify the accuracy of the numerical differentiation. In the first test we repeatedly differentiated known function representing solution of Equations (24) (Figure 6). Results shown in Figure 7 demonstrate the 8th-order accuracy of the first differentiation, the 7th-order accuracy of the second differentiation and the 6th-order accuracy of the 3rd-differentiation. In the second test, we solved Equation (24) using discretization

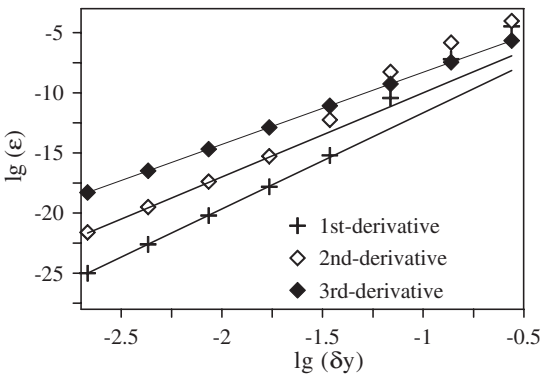

Figure 7. Variations of the error of the numerical differentiation of a known function as a function of the grid size. Conditions of the test are similar to that described in Figure 3. Exact solution of Equation (24) is used as the test function.

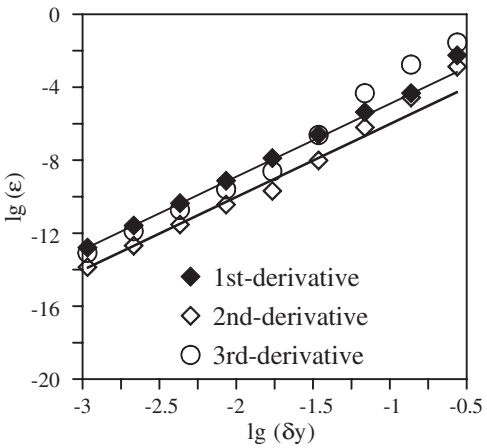

Figure 8. Variations of the error of numerical differentiation of a numerically determined solution of Equation (24) as a function of the grid size. Conditions of the test are similar to that described in Figure 7.

described above and repeatedly differentiated numerical solution. Results displayed in Figure 8 demonstrate that we maintain the 4th-order accuracy for all derivatives.

3. NUMERICAL TESTS OF THE COMPLETE ALGORITHM

A set of physical problems whose solutions have been determined using other methods has been selected to test the complete algorithm. Results are illustrated in terms of evolution of the kinetic energy associated with different Fourier modes. This energy is defined as

$$E_0 = \frac{1}{4}\int_{-1}^{1} \hat{u}_0^2 \,\mathrm{d}y, \quad E_n = \frac{1}{2}\int_{-1}^{1} (|\hat{u}_n|^2 + |\hat{v}_n|^2)\,\mathrm{d}y, \quad n \neq 0 \tag{30}$$

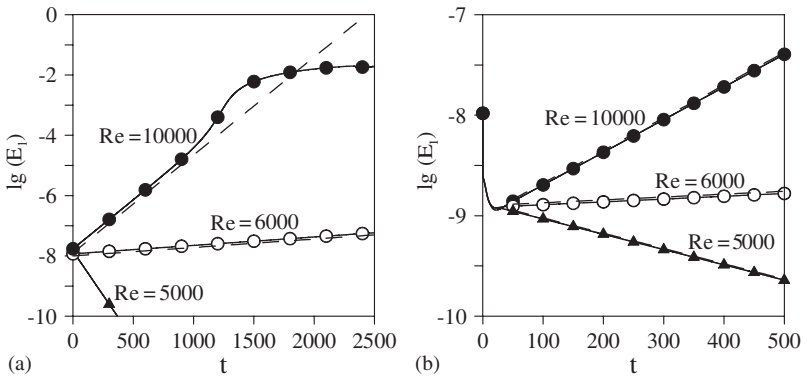

Figure 9. Evolution of the energy of disturbances in the Poiseuille flow. Dash lines show the growth described by the linear stability theory, solid lines describe DNS: (a) initial disturbance in the form of T–S wave; and (b) random initial disturbance.

3.1. Linear instability of Poiseuille flow

We shall consider two cases. In the first one we impose initial disturbance in the form of eigenfunction of the linear stability problem while in the second one we use random disturbance.

3.1.1. Initial disturbance in the form of Tollmien–Schlichting (TS) wave. At time zero we add to the flow small disturbance in the form of Tollmien–Schlichting wave. The relevant eigenfunction has been determined by solving the Orr–Sommerfeld equation using finite-difference discretization described in Section 2. Details of this solution are given in Appendix B. The amplitude of the disturbance has been selected by fixing the amplitude of the eigenfunction at such a level that the growth process is not affected by nonlinear effects. The growth/decay of the disturbance is exponential and its numerical value depends on the flow Reynolds number and the disturbance wave number. Figure 9(a) illustrates the growth of the disturbance for the subcritical, near-critical and supercritical conditions together with predictions based on the linear stability theory for the disturbance wave number $\vartheta = 1$. A very good agreement between the theory and numerical simulations is noted. The reader may note that the algorithm reproduces correct growth from the very initial moment as the initial conditions correspond exactly to the disturbance described by the linear theory. An eventual formation of the saturation state for $Re = 10\,000$ is observed.

3.1.2. Random initial disturbance. At time zero we add to the flow a random disturbance with the wave number $\vartheta = 1$. Results displayed in Figure 9(b) demonstrate that after an initial transient of about 50 time units the flow evolution follows pattern predicted by the linear stability theory. These results demonstrate that the algorithm has sufficient accuracy to capture delicate flow re-arrangement associated with the energy transfer from the random initial disturbance to the TS wave.

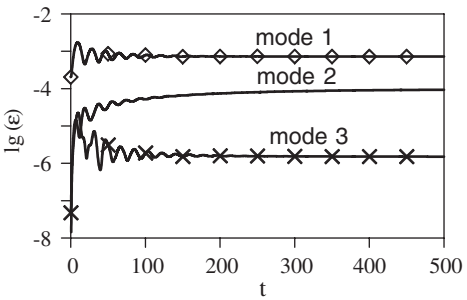

Figure 10. Evolution of energy of flow modifications associated with the wall suction for the suction amplitude $S = 0.02$, the suction wave number $\alpha = 1.025$ and the flow Reynolds number $Re = 2000$.

Table I. Comparison of the present results with those given in Reference [18] for $S = 0.02$, $\alpha = 1.025$.

Energy of Fourier modes	Present results	Reference [18] (steady solution)
Mode 0	3.1734E-6	3.1727E-6
Mode 1	1.5345E-4	1.5343E-4
Mode 2	1.3352E-7	1.3349E-7

3.2. Flow modifications induced by application of periodic suction at the lower wall

We modify the Poiseuille flow by adding distributed suction/blowing at the lower wall in such a way that the suction does not affect the net mass flow through the channel. Arbitrary suction distribution can be represented in terms of Fourier expansions [18]. In our test we shall consider suction described only by one Fourier mode, i.e. $v(x,-1) = S\cos(\alpha x)$ and we shall determine the resulting flow. When the Reynold's number is sufficiently low, i.e. $Re = 2000$, the flow modifications are expected to have a stationary form. Figure 10 displays results of simulation for $S = 0.02$, $\alpha = 1.025$. The flow has Poiseuille form initially and is disturbed by sudden imposition of suction at the initial time. The initial transient dies out after approximately 200 time units and the solution approaches steady form identical to that obtained by Floryan [18] in a steady state analysis. Additional comparisons are given in Table I.

The reader should note that this test has to be carried out at a sufficiently small Reynolds number where the flow is stable and thus all initial disturbances should eventually die out and an asymptotic steady state should be achieved. The case of flow with higher Reynolds number is considered in the next section.

3.3. Linear instability of channel flow modified by distributed wall suction

The suction-modified flow becomes unstable at higher values of Re [18] similarly as the unmodified flow discussed in Section 3.1. This process is more delicate and we wish to determine if our algorithm is able to simulate it. We shall consider two cases, i.e. the initial disturbance corresponding to the eigenfunctions of the linear stability problem and the case of a random initial disturbance.

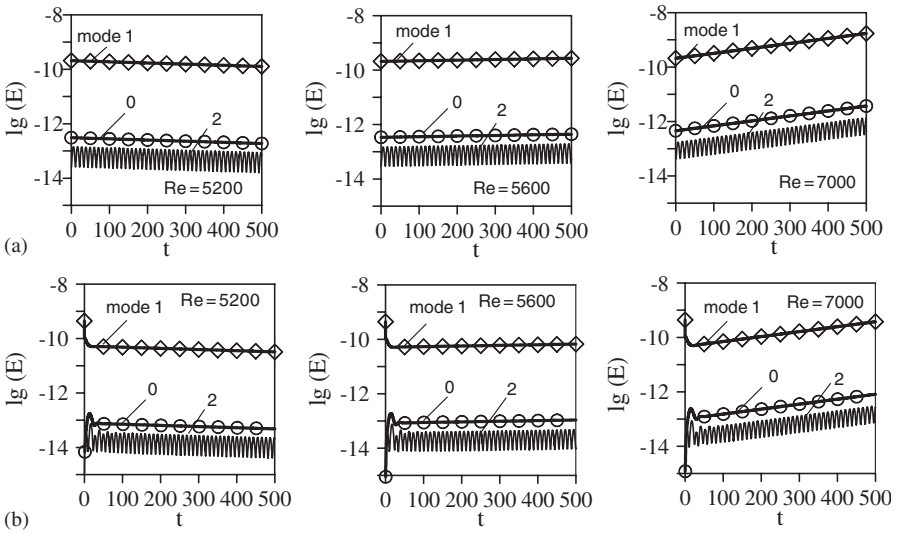

Figure 11. Evolution of the energy of disturbances in a Poiseuille flow modified by wall suction with the amplitude $S = 0.002$ for $Re = 5200, 5600$ and 7000: (a) initial disturbances in the form of eigenfunctions of the linear stability problem, $\alpha = 1.05$, $\vartheta = 1.05$; and (b) random initial disturbances, $\alpha = 1.05$, $\vartheta = 1.05$.

3.3.1. Initial disturbance in the form of eigenfunctions of the linear stability problem. We begin with the steady state form of the suction-modified-flow for the suction amplitude $S = 0.02$ and the suction wave number $\alpha = 1.025$ determined using method described in Reference [18]. At time zero we add to the flow small disturbance in the form of eigenfunctions of the linear stability problem described in Reference [18] with the disturbance wave number $\vartheta = 1.025$. Figure 11(a) illustrates evolution of the energy of disturbances for the subcritical, near-critical and supercritical cases. Good agreement with the predictions based on the linear theory is clearly visible. The reader may note the absence of any initial transient as the initial conditions correspond exactly to the linear stability problem.

3.3.2. Random initial disturbance. We begin with the steady state form of the suction-modified-flow for the suction amplitude $S = 0.02$ and the suction wave number $\alpha = 1.05$ determined using method described in Reference [18]. At time zero we add to the flow random disturbance with the wave number $\vartheta = 1.05$. Results displayed in Figure 11(b) demonstrate that after a short initial transient the flow evolution agrees with the predictions based on the linear stability.

3.4. Nonlinear instability of channel flow modified by distributed wall suction

When disturbance level reaches certain threshold, nonlinear effects come into play and disturbance growth is expected to saturate, similarly as in the case of the un-modulated flow discussed in Section 3.1. This process is illustrated in Figure 12 for $Re = 7000$, $S = 0.002$, $\alpha = \vartheta = 1.025$ and demonstrates that the present algorithm is able to reproduce qualitative

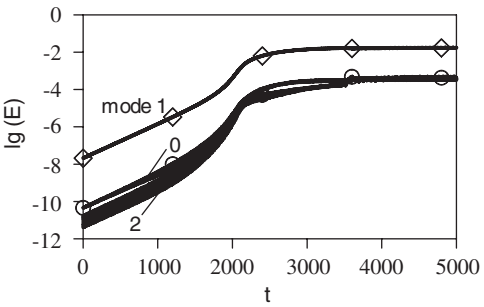

Figure 12. Nonlinear growth of disturbances in a Poiseuille flow in a channel modified by wall suction with the amplitude $S = 0.002$ and the wave number $\alpha = 1.05$ for the flow Reynolds number $Re = 7000$.

features of the saturation process. Verification of the quantitative features must wait for the development of the required nonlinear stability theory.

4. EXTENSION TO THREE DIMENSIONS

The present algorithm can be easily extended to three-dimensional flows [17]. Consider channel as shown in Figure 1 that extends to $\pm\infty$ in the spanwise z-direction. The three-dimensional flow equations can be expressed as

$$\frac{\partial}{\partial t}(\nabla^2 v) = \frac{1}{Re}\nabla^2(\nabla^2 v) + N_v \tag{31}$$

$$\frac{\partial \eta}{\partial t} = \frac{1}{Re}\nabla^2 \eta + N_\eta \tag{32}$$

where $\eta = \partial u/\partial z - \partial w/\partial x$ is the wall-normal vorticity component, u, v and w are the velocity components in the x-, y- and z-directions, respectively, and N_v and N_η are nonlinear terms whose explicit forms are given in Appendix C. The flow is assumed to be periodic the spanwise and streamwise directions and the flow quantities (e.g. $u, v, w, uu, uv, uw, vv, vw, ww, \eta$) are expressed in the form of Fourier expansions, e.g.

$$\overline{v}(x, z, y, t) = \overline{v}_0(y) + \sum_{n=-\infty}^{+\infty}\sum_{l=-\infty}^{+\infty} \hat{\overline{v}}_{nl}(y, t)\mathrm{e}^{\mathrm{i}(\alpha n x + \beta l z)} \tag{33}$$

where $\alpha = 2\pi/\lambda_x$, $\beta = 2\pi/\lambda_z$ and λ_x and λ_z denote wavelengths in the streamwise and spanwise directions, respectively. The modal functions are described by following equations:

$$\frac{\partial}{\partial t}[(D^2 - k_{\mathrm{nl}}^2)\hat{v}_{\mathrm{nl}}] = \frac{1}{Re}[D^4(\hat{v}_{\mathrm{nl}}) - 2k_{\mathrm{nl}}^2 D^2(\hat{v}_{\mathrm{nl}}) + k_{\mathrm{nl}}^4 \hat{v}_{\mathrm{nl}}] + \hat{N}_v \tag{34}$$

$$\frac{\partial \hat{\eta}_{\mathrm{nl}}}{\partial t} = \frac{1}{Re}[(D^2 - k_{\mathrm{nl}}^2)\hat{\eta}_{\mathrm{nl}}] + \hat{N}_\eta \tag{35}$$

where $\hat{N}_v$ and $\hat{N}_\eta$ represent the nonlinear terms and their explicit forms are given in Appendix C. Each of the above equations can be solved separately using time discretization described in Section 2.3, as the nonlinear coupling terms are evaluated explicitly. Equation (34) is qualitatively similar to Equation (10a) and thus the discretization method described in Section 2.4 can be applied directly. Equation (35) is only second-order and can be easily discretized using similar technique.

5. CONCLUDING REMARKS

A method for the direct numerical solution of the unsteady form of the Navier–Stokes equations has been introduced. The method is based on a hybrid, spectral and higher-order finite-difference scheme for the spatial discretization and a three-step hybrid Runge–Kutta/Crank–Nicholson low-storage scheme for the temporal discretization. The method is described in the context of two-dimensional flows using streamfuncrion formulation of the governing equations. The finite-difference discretization is based on a nonuniform grid. The coupled system of discretization coefficients for the 4th, 2nd and 1st derivatives is determined numerically. Difficulties associated with the numerical solution of the associated ill-posed linear algebraic system are bypassed using an arbitrary accuracy arithmetic. Such procedure has to be carried only once at the beginning of the computations and thus the additional costs are minimal in comparison with the total cost of the computations. The evaluations of the higher derivatives in nonlinear terms is carried out using an implicit, higher-order, compact differentiation procedure; the required discretization coefficients have been determined numerically using an arbitrary accuracy arithmetic. Extensive testing shows that the finite-difference scheme delivers the 4th-order accuracy. It has been demonstrated that the algorithm is able to reproduce delicate processes associated with the growth of disturbances in parallel shear layers as well as in spatially-modulated shear layers. The proposed method can be easily generalized to more complex equations as the numerical process employed eliminates the need for the explicit evaluations of the coefficients of the finite-diference quotients. Extensions to three-dimensional flow equations are also given.

APPENDIX A: BOUNDARY VALUE PROBLEMS AT FRACTIONAL TIME STEPS

A.1. Equations for the fractional time step $t = m + 1/3$ for mode n

The coefficients of the boundary value problem (12) have the following form:

$$b_1 = -\tau_1/Re \tag{A1a}$$

$$b_2 = -1/\Delta t - (\tau_1/Re)(i\alpha ncRe - 2\alpha^2 n^2) \tag{A1b}$$

$$b_3 = 0 \tag{A1c}$$

$$b_4 = -\alpha^2 n^2/\Delta t - (\tau_1/Re)(\alpha^4 n^4 - ic\alpha^3 n^3 Re) \tag{A1d}$$

$$g(y) = \{(D^2-\alpha^2n^2)/\Delta t + (\kappa_1/Re)[D^4 + (i\alpha ncRe-2\alpha^2n^2)D^2 + \alpha^4n^4-ic\alpha^3n^3Re]\}\hat{\varphi}_n^{(m)} + \gamma_1\hat{H}_n^{(m)} \tag{A1e}$$

where $\hat{H}_n^{(m)} = i\alpha n[i\alpha n(\langle u\hat{v}\rangle_n^{(m)}) + D(\langle v\hat{v}\rangle_n^{(m)})]-i\alpha nD(\langle u\hat{u}\rangle_n^{(m)})-D^2(\langle u\hat{v}\rangle_n^{(m)})$. The boundary conditions are as follows:

$$\text{at } y=-1: \hat{\varphi}_n^{(m+1/3)}(-1, m+\tfrac{1}{3}) = \left[\frac{i(\hat{g}_1)_n e^{i\alpha nc(m+1/3)\Delta t}}{n\alpha}\right]^{(m+1/3)} \quad \text{for } n\neq 0$$

$$\hat{\varphi}_0^{(m+1/3)}(-1, m+\tfrac{1}{3}) = 0 \tag{A1f}$$

$$\text{at } y=1: \hat{\varphi}_n^{(m+1/3)}(1, m+\tfrac{1}{3}) = \left[\frac{i(\hat{g}_2)_n e^{i\alpha nc(m+1/3)\Delta t}}{n\alpha}\right]^{(m+1/3)} \quad \text{for } n\neq 0$$

$$\hat{\varphi}_0^{(m+1/3)}(1, m+\tfrac{1}{3}) = Q - \tfrac{4}{3} \tag{A1g}$$

$$\text{at } y=\pm 1: \frac{d\hat{\varphi}_n^{(m+1/3)}}{dy} = 0 \tag{A1h–i}$$

A.2. Equations for the fractional time step $t = m + \frac{2}{3}$ for mode n

The coefficients of the boundary value problem (12) have the following form:

$$b_1 = -\beta_2/Re \tag{A2a}$$

$$b_2 = -1/\Delta t-(\tau_2/Re)(i\alpha ncRe-2\alpha^2n^2) \tag{A2b}$$

$$b_3 = 0 \tag{A2c}$$

$$b_4 = -\alpha^2n^2/\Delta t-(\tau_2/Re)(\alpha^4n^4-ic\alpha^3n^3Re) \tag{A2d}$$

$$g(y) = \{(D^2-\alpha^2n^2)/\Delta t + (\kappa_2/Re)[D^4 + (i\alpha ncRe-2\alpha^2n^2)D^2 + \alpha^4n^4-ic\alpha^3n^3Re]\}\hat{\varphi}_n^{(m+1/3)} + \gamma_2\hat{H}_n^{(m+1/3)} + \xi_1\hat{H}_n^{(m)} \tag{A2e}$$

where $\hat{H}_n^{(m)} = i\alpha n[i\alpha n(\langle u\hat{v}\rangle_n^{(m)}) + D(\langle v\hat{v}\rangle_n^{(m)})]-i\alpha nD(\langle u\hat{u}\rangle_n^{(m)})-D^2(\langle u\hat{v}\rangle_n^{(m)})$ and $\hat{H}_n^{(m+1/3)} = i\alpha n[i\alpha n(\langle u\hat{v}\rangle_n^{(m+1/3)}) + D(\langle v\hat{v}\rangle_n^{(m+1/3)})]-i\alpha nD(\langle u\hat{u}\rangle_n^{(m+1/3)})-D^2(\langle u\hat{v}\rangle_n^{(m+1/3)})$. The boundary conditions are as follows:

$$\text{at } y=-1: \hat{\varphi}_n^{(m+2/3)}(-1, m+\tfrac{2}{3}) = \left[\frac{i(\hat{g}_1)_n e^{i\alpha nc(m+2/3)\Delta t}}{n\alpha}\right]^{(m+2/3)} \quad \text{for } n\neq 0$$

$$\hat{\varphi}_0^{(m+2/3)}(-1, m+\tfrac{2}{3}) = 0 \tag{A2f}$$

$$\text{at } y=1: \hat{\varphi}_n^{(m+2/3)}(1,m+\tfrac{2}{3}) = \left[\frac{i(\hat{g}_2)_n e^{i\alpha nc(m+2/3)\Delta t}}{n\alpha}\right]^{(m+2/3)} \quad \text{for } n\neq 0$$

$$\hat{\varphi}_0^{(m+2/3)}(1,m+\tfrac{2}{3}) = Q-\tfrac{4}{3} \tag{A2g}$$

$$\text{at } y=\pm 1: \ \frac{d\hat{\varphi}_n^{(m+2/3)}}{dy}=0 \tag{A2h–i}$$

A.3. Equations for the fractional time step $t=m+1$ for mode n

The coefficients of the boundary value problem (12) have the following form:

$$b_1 = -\tau_3/Re \tag{A3a}$$

$$b_2 = -1/\Delta t - (\tau_3/Re)(i\alpha ncRe - 2\alpha^2 n^2) \tag{A3b}$$

$$b_3 = 0 \tag{A3a–c}$$

$$b_4 = -\alpha^2 n^2/\Delta t - (\tau_2/Re)(\alpha^4 n^4 - ic\alpha^3 n^3 Re) \tag{A3d}$$

$$g(y) = \{(D^2-\alpha^2 n^2)/\Delta t + (\kappa_3/Re)[D^4 + (i\alpha cRe - 2\alpha^2 n^2)D^2 + \alpha^4 n^4 - ic\alpha^3 n^3 Re]\}\hat{\varphi}_n^{(m+2/3)} + \gamma_3 \hat{H}_n^{(m+2/3)} + \xi_2 \hat{H}_n^{(m+1/3)} \tag{A3e}$$

The boundary conditions are as follows:

$$\text{at } y=-1: \hat{\varphi}_n^{(m+1)}(-1,m+1) = \left[\frac{i(\hat{g}_1)_n e^{i\alpha c(m+1)\Delta t}}{n\alpha}\right]^{(m+1)} \quad \text{for } n\neq 0$$

$$\hat{\varphi}_0^{(m+1)}(-1,m+1) = 0 \tag{A3f}$$

$$\text{at } y=1: \hat{\varphi}_n^{(m+1)}(1,m+1) = \left[\frac{i(\hat{g}_2)_n e^{in\alpha c(m+1)\Delta t}}{n\alpha}\right]^{(m+1)} \quad \text{for } n\neq 0$$

$$\hat{\varphi}_0^{(m+1)}(1,m+1) = Q-\tfrac{4}{3} \tag{A3g}$$

$$\text{at } y=\pm 1: \ \frac{d\hat{\varphi}_n^{(m+1)}}{dy}=0 \tag{A3h–i}$$

APPENDIX B: NUMERICAL SOLUTIONS OF THE ORR–SOMMERFELD EQUATION

The linear stability problem for the Poiseuille flow is described by the Orr–Sommerfeld equation in the form

$$(i\vartheta Re)^{-1}(D^2-\vartheta^2)^2\phi = (u_0-\sigma)(D^2-\vartheta^2)\phi - D^2 u_0 \phi \tag{B1a}$$

with the boundary conditions

$$\varphi = 0, \quad \mathrm{d}\varphi/\mathrm{d}y = 0 \quad \text{at } y = \pm 1 \tag{B1b–e}$$

where ϑ denotes the disturbance wave number, σ stands for the complex frequency, $\vartheta\sigma$ denotes the complex growth rate, φ describes the disturbance stream function and u_0 denotes the streamwise velocity of the Poiseuille flow. Problem (B1) represents a 4th-order boundary value problem with a structure very similar to the structure of equations obtained for each fractional step (see Equation (12)). Equation (B1a) has to be re-arranged to the form

$$\begin{aligned}&[(i\vartheta Re)^{-1}D^4\varphi - 2\vartheta(iRe)^{-1}D^2\varphi - D^2(u_0\varphi) + 2D(Du_0\varphi)]\\ &+[\vartheta^3(iRe)^{-1} + \vartheta^2 u_0]\varphi = -\sigma(D^2-\beta^2)\varphi\end{aligned} \tag{B2}$$

before our finite-difference scheme can be applied. Equation (B2) represents an eigenvalue problem for the complex growth rate σ where φ denotes the corresponding eigenvector. Discretization of derivatives converts the above problem to a matrix eigenvalue problem, which can be solved using standard techniques.

APPENDIX C

The nonlinear terms in Equations (31)–(32) have the following forms:

$$N_v = \left(\frac{\partial}{\partial x^2} + \frac{\partial}{\partial z^2}\right)H_v - \frac{\partial}{\partial y}\left(\frac{\partial H_u}{\partial x} + \frac{\partial H_w}{\partial z}\right), \quad N_\eta = \frac{\partial H_u}{\partial z} - \frac{\partial H_w}{\partial x}$$

where

$$H_u = \frac{\partial(\langle uu\rangle)}{\partial X} + \frac{\partial(\langle uv\rangle)}{\partial y} + \frac{\partial(\langle uw\rangle)}{\partial z}, \quad H_v = \frac{\partial(\langle vu\rangle)}{\partial X} + \frac{\partial(\langle vv\rangle)}{\partial y} + \frac{\partial(\langle vw\rangle)}{\partial z}$$

$$H_w = \frac{\partial(\langle wu\rangle)}{\partial X} + \frac{\partial(\langle wv\rangle)}{\partial y} + \frac{\partial(\langle ww\rangle)}{\partial z}$$

The nonlinear terms in Equations (33) and (34) have the form

$$\hat{N}_v = k_{\mathrm{nl}}^2(\hat{H}_v)_{\mathrm{nl}} - D[i\alpha n(\hat{H}_u)_{\mathrm{nl}} + i\beta l(\hat{H}_w)_{\mathrm{nl}}], \quad \hat{N}_\eta = i\beta l(\hat{H}_u)_{\mathrm{nl}} - i\alpha n(\hat{H}_w)_{\mathrm{nl}}$$

where

$$(\hat{H}_u)_{\mathrm{nl}} = i\alpha n\langle\hat{u}\hat{u}\rangle_{\mathrm{nl}} + D\langle\hat{u}\hat{v}\rangle_{\mathrm{nl}} + i\beta l\langle\hat{u}\hat{w}\rangle_{\mathrm{nl}}, \quad (\hat{H}_v)_{\mathrm{nl}} = i\alpha n\langle\hat{u}\hat{v}\rangle_{\mathrm{nl}} + D\langle\hat{v}\hat{v}\rangle_{\mathrm{nl}} + i\beta l\langle\hat{v}\hat{w}\rangle_{\mathrm{nl}}$$

$$(\hat{H}_w)_{\mathrm{nl}} = i\alpha n\langle\hat{u}\hat{w}\rangle_{\mathrm{nl}} + D\langle\hat{w}\hat{v}\rangle_{\mathrm{nl}} + i\beta l\langle\hat{w}\hat{w}\rangle_{\mathrm{nl}}$$

The notation used is analogous to that introduced in Section 2.

ACKNOWLEDGEMENTS

This work has been supported by the NSERC of Canada. The authors wish to thank Drs M. Quadrio and P. Lucini for their assistance. Sharcnet provided the required computing resources.

REFERENCES

1. Canuto C, Hussaini MY, Quarteroni A, Zang TA. *Spectral Methods in Fluid Dynamics*. Springer: Berlin, 1987.
2. Gottlieb D, Orszag SA. *Numerical Analysis of Spectral Methods*. Society for Industrial and Applied Mathematics (SIAM): Philadelphia, PA, 1977.
3. Lele SK. Compact finite-difference schemes with spectral-like resolution. *Journal of Computational Physics* 1992; **103**:16–42.
4. Karniakadis GE. Spectral element simulations of laminar and turbulent flows in complex geometries. *Applied Numerical Mathematics* 1989; **6**:85–105.
5. Patera AT. A spectral element method for fluid dynamics: laminar flow in a channel expansion. *Journal of Computational Physics* 1984; **54**:468–488.
6. Kwok WY, Moser RD, Jimenez J. A critical evaluation of the resolution properties of B-spline and compact finite-difference methods. *Journal of Computational Physics* 2001; **174**:510–551.
7. Hirsh RS. Higher order accurate difference solutions of fluid mechanics problems by a compact finite differencing technique. *Journal of Computational Physics* 1975; **19**:90–109.
8. Rubin SG, Koshla PK. Polynomial interpolation methods for viscous flow calculations. *Journal of Computational Physics* 1977; **24**:217–244.
9. Mahesh K. A family of high-order finite-difference schemes with good spectral resolution. *Journal of Computational Physics* 1998; **145**:332–358.
10. Sadri R, Floryan JM. Entry channel flow. *Computers and Fluids* 2002; **31**:133–157.
11. Rokicki J, Floryan JM. Domain decomposition and the compact fourth-order algorithm for the Navier–Stokes equations. *Journal of Computational Physics* 1995; **116**:79–96.
12. Rokicki J, Floryan JM. Higher-order unstructured domain decomposition method for the Navier–Stokes equations. *Computers and Fluids* 1999; **28**:87–120.
13. Spalart PR, Moser RD, Rogers MM. Spectral methods for the Navier–Stokes equations with one infinite and two periodic directions. *Journal of Computational Physics* 1991; **96**:297–324.
14. Quadrio M, Luchini P. Direct numerical simulation of the turbulent flow in a pipe with annular cross-section. *European Journal of Mechanics B/Fluids* 2002; **21**:413–427.
15. Quadrio M, Luchini P. Integral space-time scales in turbulent wall flows. *Physics of fluids* 2003; **15**:2219–2227.
16. Williamson JH. Low-storage Runge–Kutta schemes. *Journal of Computational Physics* 1980; **35**:48–56.
17. Quadrio M, Luchini P, Floryan JM. A parallel algorithm for the direct numerical simulation of turbulent channel flow. *Proceedings of the 11th Annual Conference of the CFD Society of Canada*, Vancouver, Canada, 28–30 May 2003, 710–711.
18. Floryan JM. Stability of wall-bounded shear layers in the presence of simulated distributed surface roughness. *Journal of Fluid Mechanics* 1997; **335**:29–55.

